Polar Science 30 (2021) 100732

Contents lists available at ScienceDirect

Polar Science

journal homepage: www.elsevier.com/locate/polar

Modelling the seasonal variations of soil temperatures in the Arctic coasts

Mohammad Akhsanul Islam [a,*], Raed Lubbad [a], Seyed Ali Ghoreishian Amiri [a], Vladislav Isaev [b], Yaroslav Shevchuk [b], Alexandra Vladimirovna Uvarova [c], Mohammad Saud Afzal [d], Avinash Kumar [e]

[a] Civil and Environmental Engineering Department, Norwegian University of Science and Engineering (NTNU), Norway
[b] Department of Geocryology, Lomonosov Moscow State University (MSU), Russia
[c] Vernadsky Institute of Geochemistry and Analytical Chemistry of RAS, Russia
[d] Department of Civil Engineering, Indian Institute of Technology, Kharagpur, India
[e] National Center for Polar and Ocean Research (NCPOR), Goa, India

ARTICLE INFO

Keywords:
Soil temperature
Arctic coastal erosion
Thermodenudation
Permafrost thawing

ABSTRACT

The soil temperature within the Arctic coasts within the continuous permafrost is not widely measured; the temporal and spatial resolutions of the measured temperature observations are relatively high. In this study, we examined the methods to interpolate, hindcast and forecast temperature measurements within the active layer and shallow permafrost when the temperature measurements at the surface or near the surface are available. The temperature variations along the year are periodic, and hence attempts are made to express the seasonal variations with a combination of periodic function (Fourier components); which are used as boundary conditions to reach the analytical solutions. The temperature measurements from surface to about 10 metre of depths at the Baydaratskaya Bay, Kara Sea are available. We adopted a data-driven model based on simplified analytical closed-form solution derived from the boundary conditions. The parameters of the solution are calibrated from the field measurements and validated with field observations. The model then can be used to hindcast and forecast temperature at any points within the soil.

1. Introduction

The erosion of the Arctic coasts reflects the complex interaction between climate, coastal morphology and geology in which the unique environmental conditions related to permafrost are subject to thermal and mechanical instability (Are, 1988). Field observations identified various erosion mechanisms such as a bluff failure by niche erosion (thermoabrasion), bluff face thaw (thermodenudation), retrogressive slumping processes in the Arctic coasts, either separately or in combinations (Vijay et al., 2018). The models by Nairn et al. (1998), Kobayashi et al. (1999), Leont'yev (2003, 2004), Hoque and Pollard (2009), Ravens et al. (2012) and Barnhart et al. (2014) describe the Arctic coastal erosion as an effect of the hydrodynamic and thermal driving forces on standardised one-dimensional (1D) or two-dimensional (2D) coastal profiles to simulate coastal erosion because of the thermoabrasion process. Thermal energy transfer based on air–water–soil temperature profiles, thawing of permafrost and the degradation of the mechanical strength of the soil are ignored in most of the existing conceptual models (Lantuit and Pollard, 2008). Comprehensive models of coastal erosion, including the effects of the thermodenudation process, have not yet been developed (Vijay et al., 2018). Meanwhile, observations from the various Arctic coasts suggest that the ongoing and foreseen thermokarst activities lead to considerable erosion by thermodenudation. For example, we expect the thawing of permafrost to increase unprecedentedly in connection with the effects of climate warming (Lewkowicz, 1991). Temperature increase within permafrost will lead to an increased rate of thawing of soil ice and may speed up Arctic coastal erosion (Bernstein et al., 2008).

The permafrost is linked with the surrounding atmosphere by an active layer, vegetation and snow covers which may vary enormously with time and location (Romanovsky and Osterkamp, 1997). The active layer thickness (or the depth of the seasonal thawing) is usually estimated from satellite images, from in-situ measurements or using some semi-analytical formula. The semi-analytical formulas are based on a functional relationship between thawing depth, air temperatures and the soil's thermal properties (Lantuit and Pollard, 2008). The Stefan-type equations ($x = m \cdot \sqrt{T_{index}}$ where T_{index} is the thawing index, m is related to thermal properties of soil, and x is the thawing depth) are widely used to predict the depth of permafrost thawing or to estimate the thermodenudation rate (Romanovsky and Osterkamp, 1997). Similar simplified analytical solutions or empirical relations between the

* Corresponding author.
E-mail address: mohammad.a.islam@ntnu.no (M.A. Islam).

https://doi.org/10.1016/j.polar.2021.100732
Received 9 November 2020; Received in revised form 26 July 2021; Accepted 27 July 2021
Available online 11 August 2021

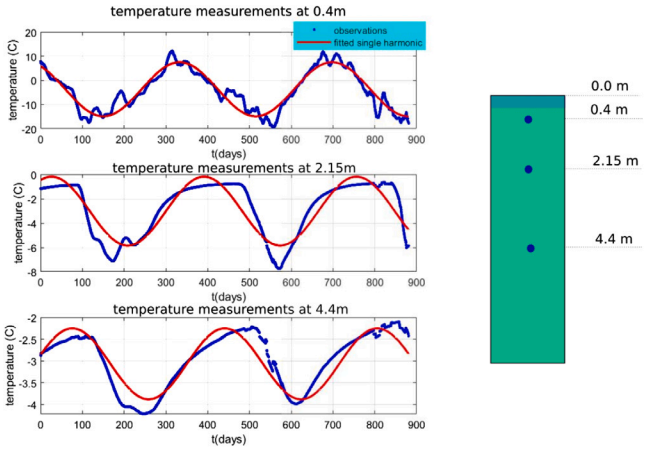

Fig. 1. The time-series of temperatures at a depth of 0.4 m, 2.15 m and 4.4 m are shown. The blue dots are observations at 12 h intervals. The total length of the observations is about 880 days. A sine-wave function is fitted (marked by the red line) using the least square error method. The soil at the depth of 4.4 m never reaches the unfrozen phase, i.e. temperature always remains below zero. (For interpretation of the references to colour in this figure legend, the reader is referred to the web version of this article.)

thawing depth and temperature measurements are also applied (Guégan, 2015; Romanovsky and Osterkamp, 1997). Limitations of all the above formulas are: (a) unable to model temporal and spatial variation of the soil temperatures, (b) the models are forced to use spatial- and temporal-averaged values of temperature and (c) restricted to assume constant thawing/freezing temperatures regardless of the variations in the soil properties (e.g. effect of the salinity, organic matter on the freezing temperature cannot be assessed) (Guégan, 2015). Only continuous and high resolution (both temporal and spatial) soil temperature profiles can solve the aforementioned limitations. Unlike other environmental parameters, we rarely measure the soil temperature on a regular basis (Holmes et al., 2008).

In this study, we adopt analytical closed-form solution to describe the temporal variation of the soil temperatures at various depths (we focus on the active layer and the shallow permafrost from 0.5 m to 10 m). We base the solution on the classical 1D heat convection–diffusion equation to describe the heat transfer in the soil with boundary conditions assuming temporal temperature variation at the air–soil interface to be periodic. The temperature variation at the soil surface expressed as a harmonic function is a suitable boundary condition to depict the seasonal variations. The combinations of the multiple harmonic functions can capture variations with higher accuracy and prediction errors are smaller. We proceed by calibrating and validating the solution against various consecutive years (from 2014 to 2018) of continuous full-scale data of soil temperatures (from 0 metre to 9.9 m depths) at five different locations representing different geological and meteorological conditions at Baydaratskaya Bay, Kara sea, Russia. For the calibration, we use the first 80% of the data and apply machine learning algorithms to estimate parameters like temperature wave-amplitude reduction rate, temperature wave-phase lag, soil thermal diffusivity and liquid water flux density. The remaining observations are used for the validation of calibrated solutions. The calibrated and validated solutions for the Arctic coasts presented in this paper may be used to (1) hindcast, and forecast soil temperatures at various depths of the soil on the basis of temperature measurement at or near the surface, (2) estimate the thawing depth and thawing rates during the summer and refreezing during the winter; taken into account the variation of the freezing/thawing temperatures with the soil properties, and (3) improve the understanding of the thermodenudation initiation process and hence improve the capabilities of Arctic coastal erosion models.

2. Seasonal variation of temperature in the Arctic coasts

In this section, we use full-scale observations to establish an understanding of the problem. A comprehensive description of the full-scale data is provided in Section 3.3. Here, we present one temperature profile (see Fig. 1) only as a sample of the measurements.

Fig. 1 shows temperature measurements at three different depths, i.e., at 0.4 m, 2.15 m, and 4.4 m. The three temperature measurements are about 880 days, which means each time series consists of at least two summers and two winters. Each of the three chosen observations represents a certain layer of the soil in the Arctic. Typically, the active layer on which some vegetation can be seen is 0.5 m to 1 metre deep. The layer below the active organic layer is the transitional active layer. It is low on organic material; but subject to annual freezing and unfreezing, i.e. during summer, the soil is free of ice. The layer at 4.4 m is permafrost. The temperature at the permafrost layer never rises more than zero degrees, i.e. during summer, the layer stays frozen.

A sine-wave is fitted on each of the observations (red line). Attempts are made to represent the seasonal temperature variations with a single harmonic function. One of the earliest model is the sine-wave model, where the periodical temperature changes are described using a single harmonic function (a sine function with time period of 365 days). Van Wijk and De Vries (1963) and Andersland et al. (2003), proposed the following equation to express the temperature variation at any depth in the soil:

$$T_g(z,t) = T_m(z) + T_a(z) \cdot sin(2\pi t f + \phi(z)) \tag{1}$$

where T_m is the mean temperature, T_a is the amplitude of the harmonic sine wave, f is the frequency of the wave, f interchangeable with ω $(= 2\pi f)$ -the angular frequency, ϕ is the phase of the wave. As shown in the Fig. 1, the amplitude, T_a and the phase, ϕ are different at two depths but the frequency, f remains the same. When Eq. (1) is applied to Arctic coasts temperature measurements (as shown in Fig. 1) where temperature variations also follow a periodical cycle, some deviations are noticed. The errors of fitting a sine-waves are prominent close to the peaks, which are again greater at a depth of 2.15 m when compared with 0.4 m and 4.4 m of depth. According to our understanding, the significant cause of such deviations is due to the requirement of latent heat of phase-change. The effect of phase change on the deviations are (1) delay in reaching the peak and (2) sometimes slightly lower amplitude at the peaks.

To model the above observations, one can in principle solve the heat balance equation in porous medium as shown in Eq. (2) with boundary and initial conditions (Plaxis, 2021).

$$\frac{\partial}{\partial t}\left(nS\rho_w e_w + n(1-S)\rho_v e_v + (1-n)\rho_s e_s\right) = -\nabla \cdot \left(\underline{J}_w + \underline{J}_v\right) + Q_T \tag{2}$$

where e_w, e_v and e_s are the internal energy in the water, vapour and solid phases, Q_T is the heat source term, $\underline{J}_w$ and $\underline{J}_v$ are the advective internal energy flux in water, vapour and soil (porous medium), n is porosity of the soil, ρ_w, ρ_v and ρ_s are the density of the water, vapour and soil.

It is possible to solve Eq. (2) numerically, but one has to pay special attention to the phase change and enforce the right conditions at the moving boundary. We use the software Plaxis to solve Eq. (2). Plaxis is a commercial finite element software developed to model geotechnical problems. The software features 2D deformation and stability analysis. It also includes a module that offers to simulate geothermal effects, heat flow within the soil, temperature distributions and phase change. The software can simulate temperature-dependent water properties which enables it to simulate permafrost in the Arctic coasts (Plaxis, 2021).

As a boundary condition, the temperature measurements at 0.4 and 4.4 m are used and analyses are performed to simulate the temperature profile at 2.15 m. The numerical model is based on the porous medium's heat balance equation, including the major thermal processes such as conduction, convection by water and mass balance with phase

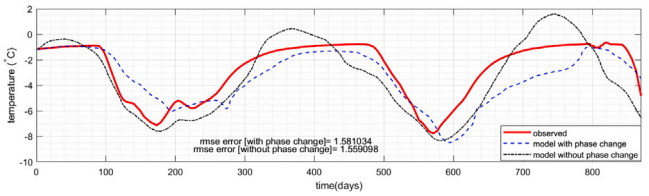

Fig. 2. The numerical modelling using Plaxis. The observations at the 0.4 m and 4.4 m are used as a boundary condition. The model estimates the temperature at the 2.15 m depth. The estimated observations are then compared with the available observation.

changes, non-isothermal deformation, soil freezing, and unfreezing. Two different approaches are used, (1) considering the latent heat of phase change with measured parameters and (2) considering the depth-averaged equivalent thermal conductivity but ignoring the phase change. It is observed that the model, when not considering the heat loss and gain during a phase change, has almost the same level of error when compared with a model that considers the latent heats (Fig. 2). When a whole cycle is considered, the energy required to melt the ice within the soil's pores at the active layers returns during the freezing phase if yearly averaged water content remains constant. At a yearly averaged value, the net effect of the heat flow changes due to latent heat of ice melting is cancelled out by the release of heat during the freezing. The figure also shows that neglecting the phase change can still be a good approximation if equivalent (calibrated) soil parameters are used. From this observation, we come to one of our main hypotheses in this study, i.e., the temperature variation in the permafrost can be modelled using a data-driven approach by solving 1D one-phase heat balance equitation with calibrated soil parameters, i.e. solution to Eq. (2).

Based on this observation, a data-driven model is developed using the simplified conduction–convection equation and the analytical solution. The solution of the equation is used to train the numerical model to find out the patterns and correlations between the time series of the temperatures at various depths. The analytical solution is the guiding principle for the algorithm to seek out the correlation and establish a localised custom relation between some basic parameters to predict the temperature at various depths. In the next sections, we describe the analytical solution used which is the basis of the pattern-seeking of the machine learning algorithm.

2.1. Simplified thermal model

A typical Arctic coastal profile is shown in Fig. 3. A cliff stands at the end of a narrow beach. During the winter, the beach, bluff face and the cliff are covered with snow while the sea is covered with ice. Coastal erosion due to thermodenudation occurs during the summer after the snow is melted away. The direction of the heat transfer is downward during the summer when the air temperature is warmer than the soil temperature. The direction changes during winter as the air temperature near the surface becomes colder than the permafrost temperature. Our domain of interest is the Arctic coastal cliff and the narrow beach where thermodenudation occurs. In this study, we want to find a reliable method to estimate the temperature profiles inside the cliff and the beach, estimating the temperature on a large scale. This will allow an accurate estimate of the permafrost thawing depth and improve modelling of Arctic coastal erosion due to thermodenudation.

2.1.1. Conduction–convection heat equation

To estimate the temporal variations of the soil temperature at any depth, we idealise the problem as a one-dimensional (1D) heat transfer problem. Let us assume that points A and B are two points at different depths inside the cliff shown in Fig. 3. The distance between these two points and the coordinate system used is shown in Fig. 3. The axes x and y are assumed to be along the cross-shore and alongshore direction, respectively, the positive z-axis points to the downward direction.

2.2. Governing equation to establish a data-driven model

The 1D heat convection–diffusion equation can be used to describe the heat transfer in the soil between point A and point B. Based on the conservation of the energy, the Fourier thermal conduction and convection equation for the 1D case is expressed as: (Stallman, 1965; Gao et al., 2003, 2008),

$$\frac{\partial T(z,t)}{\partial t} = \frac{\partial^2 k(z) T(z,t)}{\partial z^2} + \frac{\partial W(z) T(z,t)}{\partial z} \tag{3}$$

where k is the thermal diffusivity (unit = $m^2 s^{-1}$) and $k = \lambda / Cg$ where λ is the thermal conductivity (unit = $Wm^{-1}C^{-1}$) and C_g is the volumetric heat capacity of the soil (unit = $Jm^{-3}C^{-1}$), W is the liquid water flux density. $W = \partial k / \partial C_w / C_g w \eta z$, $\partial k / \partial z$ is the gradient of the soil thermal diffusivity in z direction, C_w is the heat capacity of the water ($J°C^{-1}m^{-3}$), w is the liquid water velocity(m/s), η is the volumetric water content of the soil (unit-less).

Eq. (3) is used as the governing equation of the problem; the equation is valid for every point regardless of the temperature profiles. However, the equation does not count for the heat sink or source at the melting phase due to the phase change of water. As we have seen in Section 2, the effect of the phase change is the deformation of the sine wave and lag of the peak positive temperature.

2.2.1. Boundary conditions

The form of the fundamental solution of the Eq. (3) depends on the boundary conditions. For $z = \infty$ or at sufficient deep soil, the solution of the equation reaches a steady state, i.e. the effect of the surface-boundary conditions cannot be seen anymore. A time series of the temperature measurements can be applied as a boundary condition at point A. One of the properties of the heat equation is that it retains the initial shape of the boundary condition (detail example is provided in Appendix C). The time series at point A can be expressed as a known form of the function to reach the analytical solution. We considered the temperature measurements at point A ($z = z_1$) as a function of time but a combination of harmonic functions with different amplitudes and time periods. Application of the boundary condition can lead to the respective solutions of Eq. (3); presented in the next section.

2.2.2. Analytical solution: a combination of harmonic functions as boundary condition

Applying Eq. (4) as a surface boundary condition to Eq. (3) (as temperature profile at point A at a depth z), a solution to soil temperature T_z can be expressed as shown in Eq. (5) (see Verhoef et al., 1996; Hu et al., 2016):

$$T(z=0,t) = T_m(z) + \sum_{n=1}^{N} T_{a_{0_n}} \sin\left(2\pi f_n t - \phi_{0_n}\right), n = 0, 1, 2, \ldots, N \tag{4}$$

The effect of the phase changes is captured by the Fourier decomposition which a single sine wave model fails to do. The effect of change in the shape and the lag of the peak are accounted for when the time series is decomposed. Theoretically, the Fourier decomposition can be decomposed to N/2+1 number of components where N is the number of observations. The analytical solution is presented as (see Verhoef et al., 1996; Hu et al., 2016):

$$T_z(z,t) = T_m(z) + \sum_{n=1}^{N} T_{a_{0_n}} e^{\left[\frac{-W-\alpha_n}{2k}\right]z} \sin\left[2\pi f_n t - \phi_{0_n} - z\frac{\beta_n}{2k}\right] \tag{5}$$

where T_m is independent of the frequency, $T_{a_{0_n}}$ is the amplitude of each harmonic function, ϕ_{0_n} is the phase of each harmonic function at the surface. W and k are independent of the harmonic functions but dependent on depth (for simplicity, W and k are made depth-averaged), and α and β are different for each harmonic function. We can rewrite part of the Eq. (5) as follows:

$$T_a(z,t) = T_{a_0} \cdot e^{-z \cdot \sum_{n=1}^{N} RR_{FS_n}} \tag{6}$$

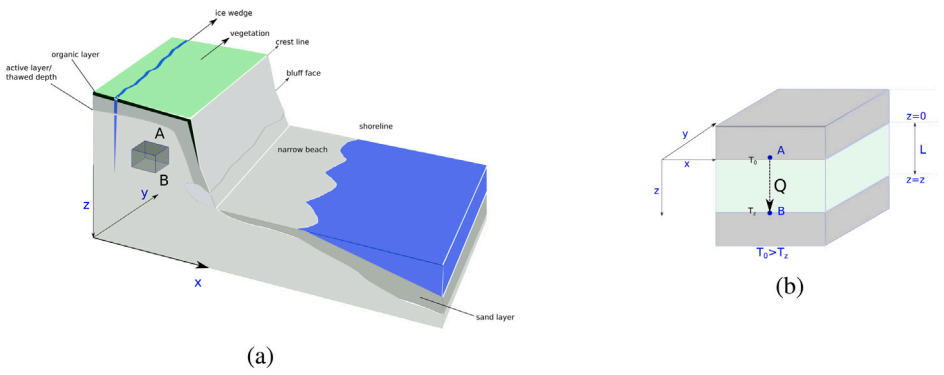

Fig. 3. (a) A typical Arctic beach at the inception of the summer is shown. The coast consists of a cliff at the end of the profile and ice-wedge polygons are visible on the cliffs. The active layer is beginning to thaw. Higher organic contents distinguish it from the rest and are situated just under the soil surface. The beach in front of the cliff is narrow, which has an elevation such that during the high tides, water does not reach the base of the bluff. (b) The heat flux between two points (A and B) inside the soil is shown. The z-axis is assumed positive towards the downwards directions, i.e. the heat flow during the summer is assumed positive. The temperature at point B (T_{z_2}) is smaller than that of point A (T_{z_1}).

Fig. 4. The study area is on an Arctic coast on the left side of the gulf of the Kara sea. The area starts from South (Latitude:68.867459N, Longitude:66.741529E) to East South (Latitude:68.842112N, Longitude 66.984593E) along the coast. The coast is straight, and the shore-normal line creates a 72° angle with the North.
Source: google earth.

$$\phi_n(z) = \phi_{0_n} - z \cdot PL_{FS_n} \tag{7}$$

where $RR_{FS_n} = \frac{-W_n - \alpha_n}{2k}$ and $PL_{FS_n} = \frac{\beta_n}{2k}$ for $n = 0, 1, 2, 3....$ The solutions are independent of the frequencies; the frequencies do not change over depth (Van Wijk and De Vries, 1963). Field observations can help to calibrate the parameters of the solution. In this paper, we use the soil temperature observations of five different locations as boundary conditions to calibrate the parameters of the Eq. (5). We used the temperatures from 0 to 9.9 m depths to calibrate the parameters: amplitude reduction rate, RR and phase lag, PL.

3. Field measurements

The soil temperature has been measured at the coast of Baydaratskaya Bay in the Kara Sea. The field investigations are completed each year, started from 2012 under the leadership of the Lomonosov Moscow State University (MSU) with support from the Centre for Research-based Innovation (CRI): Sustainable Arctic Marine and Coastal Technology (SAMCoT).

3.1. Geo-morphological description of the study area

The study area is a coast named Baydaratskaya Bay, a shallow gulf at the western side of the Kara Sea (Fig. 4). The region is inside the Arctic circle, sparsely populated and with minimal access. Although many alluvial patches, lacustrine and deposits of boggy materials are found on the coast, mostly the Pleistocene marine and Glacial sediments created the area between the Yamal Peninsula and Yugra Peninsula. We believe the area was altered by the Pleistocene ice sheets, unlike the eastern Russian coasts. Massive ice beds are present in the study area. Visible Ice wedges polygons are found along the cliffs standing at the end of the beaches and contribute to the large collapses of blocks by thermoabrasion (Ogorodov et al., 2020). The depression formed by the massive ice glaciers during the Pleistocene era developed the shallow gulf, and during the Holocene period, seawater submerged the area. The permafrost underneath the active layer is mostly continuous and reaches 30–70 m thickness. The gasoline pipe of Bovanenkovo-Uhta that transports gas to Europe passes the study area by 0.1 km in the SE direction (Isaev et al., 2019). The total length of the study area is 8 km. The river Ngoyuyaha divides the area into two almost equal parts. The Baydaratskaya bay is not the only depression along the coast of the Kara Sea; there exist many similar depressions. Some active faults bound the basin at the west side. The north part of the bay is formed during the Pleistocene and Holocene. The clay and bottom mud found in the deeper part of the bay are well-sorted, fine sands along Ural shoreface and silty sand along Yamal coast.

3.1.1. Zonal division based on cliff height: S#1 and S#2

The study area is divided into two distinct zones, marked S#1 and S#2, as shown in Fig. 5[a]. The low marine terrace with bluff heights around 4–6 m is termed zone S#1. Zone S#2 has bluff heights of 10–17 m. The S#1 and S#2 sites are about 3.5 km in the N-W direction from the cofferdam of the Bovanenkovo-Uhta gas pipeline. The study area is spread from North West (68.867459N, 66.741529E) to East South (68.842112N, 66.984593E). The zone S#1 is a low marine terrace with a length of about 4 km, starts directly from the gas pipeline (the most south-eastern point). The low terrace surface (up to 6 m) is smoothly sloping. The top surface of the cliffs is grassy with minor swamped hollows; some shallow thermokarst lakes are present, ice-wedge polygons are visible on the soil surface, we find many erosion trenches

Table 1
List of boreholes at the study area are shown. The boreholes are placed in the cliffs, both at the high and low marine terraces.

zone	Borehole ID	Depth	Coordinates	Drilled on	Remarks
S#1	bh2	9.9 m	N 68.853004 E 66.899996	Sep 2016	On the slope
S#1	bh3	9.9 m	N 68.852599 E 66.899767	Sep 2016	30 m inside the crest
S#1	bh4	6.2 m	N 68.853797 E 66.889794	Jun 2013	Inside the cliffs, discarded due to technical errors
S#1	bh5	9.9 m	N 68.858327 E 66.838207	Sep 2014	5 m above the water level
S#2	bh6	5 m [3.31 m]	N 68.857162 E 66.843057	Jun 2014	15 m above the water level

Table 2
Thermal properties of the sediments on the cliffs. The top organic active layer has very low thermal conductivity and act as a blanket hindering the thawing process. Other than the top organic layer, thermal properties vary little along the depth.

Location	Depth m	Soil type	Temperature during test °C	thermal conductivity (λ) W/(mK)
Excavation-1 N68.85305 E66.88763	0-0.15	Peat, middle stage of decomposition, dark brown	1.3	0.386
Excavation-2 N68.85361 E66.89361	0-0.20	Layering of sand light-grey, frozen and dark grey light loam, cryoturbation	1.94	0.732
	0.42–0.75	Sand, grey, fine grained, with layers of ferruginous matter	1.0	1.42
	0.40–0.60	Loam, dark grey, soft plasticity with deep decomposed organics	1.5	1.48
	0.60–0.9	Sand fine grain, light-grey with vertical band of ferruginous matter	1.15	1.16
	0.9–1.3	Sand fine grain, light-grey with vertical band of ferruginous matter	0.47	1.39
Excavation-3 N68.85277 E68.87778	0-0.30	Loam dark-grey, soft plasticity with ferruginous matter	3	1.64
	0.30–0.53	Sand light browny grey, middle grain size, with ferruginous matter layers and inclusions of fine gravel matter	1.4	1.58
	0.61–1.64	sand, light-grey, middle grain size, with horizontal layers of dark sand and vertical bands of ferruginous matter	1.13	1.04

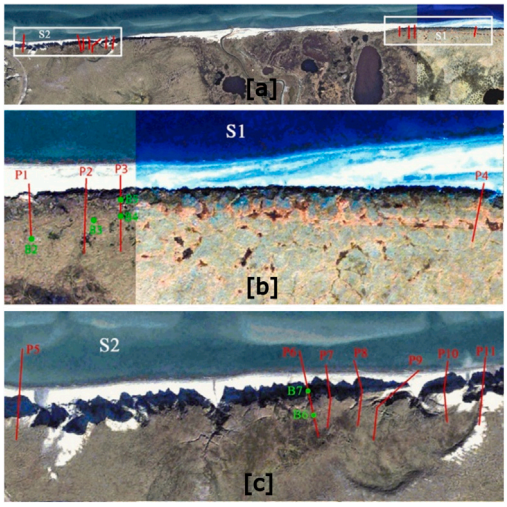

Fig. 5. The study area is divided into two zones: S#1 and S#2 identified by the bluff height differences. The longshore sediment transport exists from zone S#2 to S#1. A low lying laida separates the zones; the laida is excluded from the erosion studies. Temperature measurements at various depths are available for both the S#1 and S#2 zone.
Source: Isaev et al., 2016.

along the coastline. The bluff-heights of the S#1, from the northwest, gradually lowers and transforms into a laida of 1.5–2 m height with the Ngouyaha river valley. A laida is a low lying land in the Arctic coasts flooded during the high tides, an Arctic counterpart of the marshland found in the warmer climate. The laida shoreline is almost 1.2 km long. The laida consists of depressions with frost-thaw lakes. Some of them are drained because of the retreat of the coastline. Lake occupancy on some of the high laida areas exceeds 50%. The lower sections of the laida are followed by the S#2 zone, a more elevated terrace of 10-17 m. This S#2 zone is 4.65 km along the coastline. Deep trenches more frequently cut the surface of the S#2 with dry thermokarst lake basins (hasyrey) and younger thermokarst lakes, polygonal-shaped frost clefts and weathering spots on the sandy soil. The cliffs mostly consist of fine sediments. Unlike the sandy dune systems of the warmer climate beaches, there is no active restoration mechanism to restore the cliffs. The soil profiles of the cliffs are depicted in Fig. 6.

3.2. Soil temperature measurements

Various boreholes are constructed in the study area to measure the temperatures (list of the boreholes provided in Table 1). Initially, two boreholes were drilled, and temperature sensors were placed during field measurements of June 2013 (bh4, 6 m deep) and June 2014 (bh6, 3.5 m deep). Bh4 borehole was dug in the low terrace (S#1), and bh6 was on the high terrace (S#2). Boreholes were dug using handheld Augers, and M_log5 W (GeoPrecision GmbH) thermistors were placed inside them. A plastic pipe protects the boreholes to avoid internal collapse. The sensors of the thermistors are typically kept 0.3 m to 0.5 m apart. But near the surface, sensors are placed at 0 m and 0.1 m to capture the surface temperature. The time interval to record the data was set to be 12 h.

3.2.1. In situ thermal conductivity measurements

Lab tests of in-situ and post-work were performed to find the mechanical and thermal properties of the permafrost/cliff during the field investigation (the summary of the thermal properties are in Table 2). The experiment was performed on the cliff faces; due to the limitation of the equipment, the investigation was completed only till 1.64 m. Thermal conductivity was measured to be quite low on top of the organic active layer.

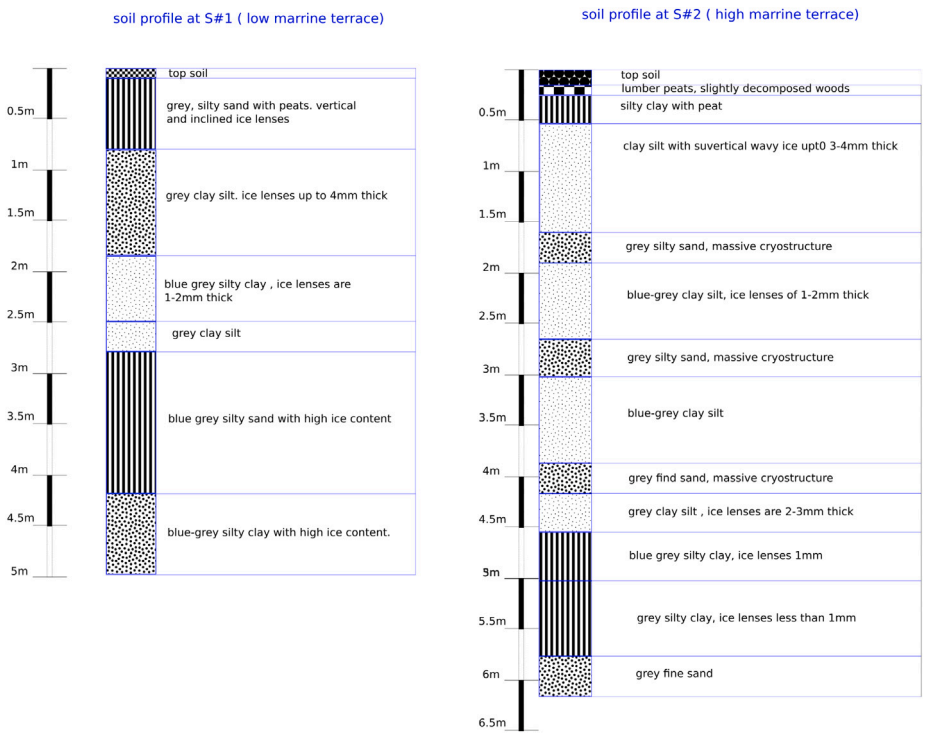

Fig. 6. Soil profiles at the two sites, S#1 and S#2. The cliffs comprise mostly fine materials. Permafrost is continuous after the depth of around 1.5 2 m. The active organic layer is thin, more or less 0.3 m and quite poor with nutrition for the vegetation (Field observation was made in Summer, 2014). Thermal conductivity of the soil is measured; presented in Table 2.

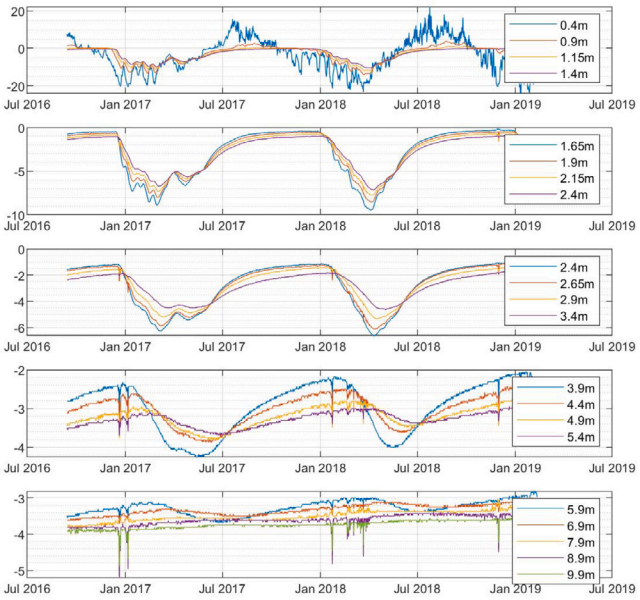

Fig. 7. Time series data of bh2: temperature measurements along with the 20 nodes from depths of 0.4 m to 9.9 m. Each sub-figure contains the data of the five depths. Some measurement anomalies are noticeable at the lower depths. However, compared to the mean values of the temperatures, the anomalies are not significant. Matlab functions 'smooth' and 'filloutliers' were used to remove the anomalies wherever required.

3.3. Field observations

We choose five sets of time series data for analysis where measurements are continuous and consistent. These observations are made throughout the year on the cliff and the beach of the Baydaratskaya.

Table 3
Summary of the temperature observations. Five time series are used for the analysis comprising temperature measurements from the zones S#1 and S#2.

Time series	Borehole ID	From	To	Total days	nodes	Depth
bh2	bh2	13-09–16	10-02–19	881	20	9.9 m
bh3	bh3	13-09–16	22-12–17	466	19	9.9 m
bh5–1	bh5	09-06–14	11-09–16	826	20	9.9 m
bh5–2	bh5	12-11–16	09-09–18	667	5	1.65 m
bh6–1	bh6	09-06–14	13-07–15	400	11	3.31 m

The earliest date of the measurements is 9 June 2014. The maximum length of the time series is 881 days (2.41 years; continuous), two periodical temperature variations are captured with the time series. The sensors measure the temperature at 12 h intervals. We lost some sensors to erosion. Moreover, temperature measurements at the deeper part of some boreholes were not appropriately captured because of some unknown sensor errors. As a result, data from all the nodes cannot be considered. The summary of the observations as time series is given in Table 3. Observations from both the high and low cliff areas (S#1 and S#2) are available. The data are re-sampled for the daily averages since the time resolution of the data is 12 h, not small enough to capture the daily temperature variation of the site. The maximum depth of the sensor was 9.9 m in both S#1 and S#2 zones. However, some anomalies are observed within the measurement due to reasons of (1) interference by local people, some strings were lost, (2) reallocation of borehole due to erosion and (3) measurement errors. To avoid the unexplained and unwanted behaviours of the measured data, parts of some time series are omitted. However, the unprocessed measurements are added in the Appendix A for references. Fig. 7 shows the time series of bh2; the rest of the time series are provided in the Appendix A.

4. Calibration of the parameters from field observation

In this study, we split the time series into two groups: training and testing data, adopting the machine learning approach. The training data

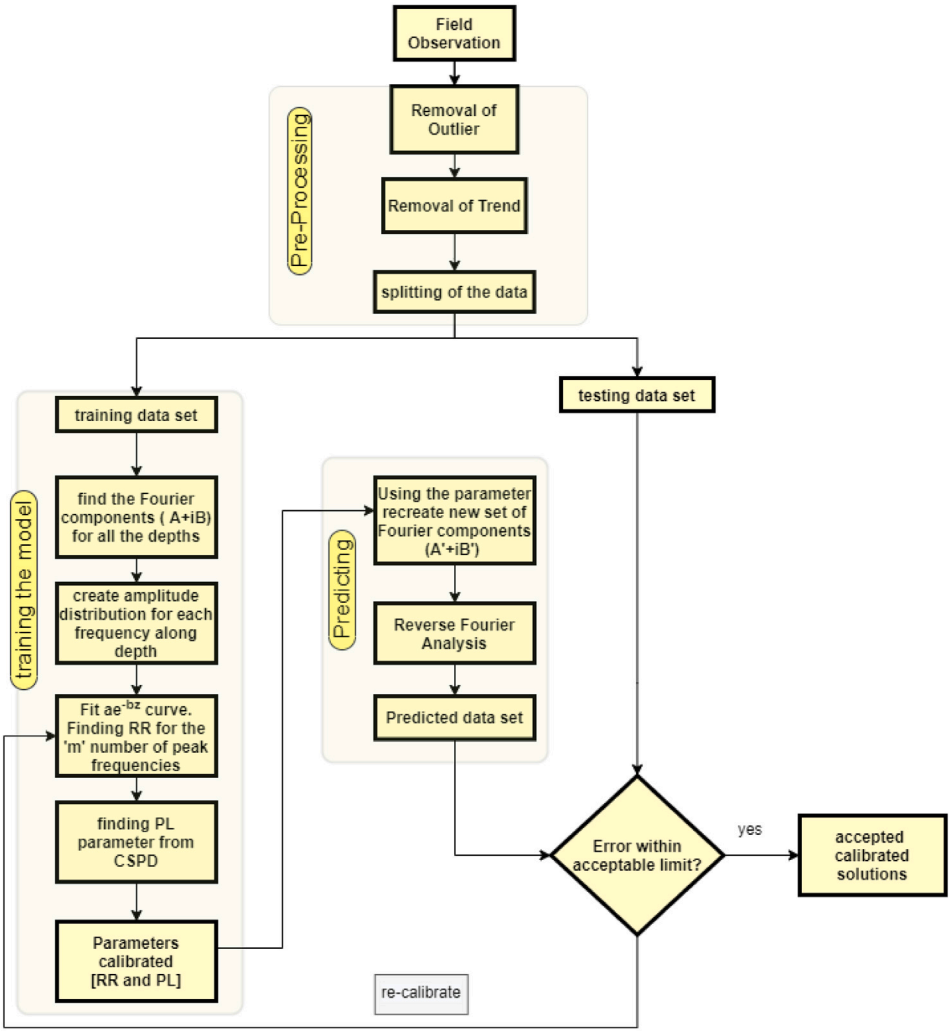

Fig. 8. The workflow of the model.

set is used to calibrate the parameters of the solutions as mentioned in Table 4,i.e. the solution is fitted to the training data set to determine the parameters (RR and PL). Thereafter, the calibrated solutions are used to numerically reproduce the remaining data, i.e. the testing data set. The calibration accuracy is determined by comparing the numerical prediction with the measurements, and the decision is made whether to accept the calibration or to re-calibrate the parameters. If the error is within the limit, the calibrated equation can be used as the governing equations to hindcast or forecast soil temperatures for the specific local area. The workflow of the methodology is shown in Fig. 8.

4.1. Pre-processing of the raw data

The field measurements contain some values which are clearly an error in the sensor. Before proceeding, these values were identified and cleared. Unusual values can greatly affect the quality of curve fitting. A trend within the time series may be observed. Since a trend is not considered when we sought the analytical solution, the trend must be removed before the calibrations.

4.1.1. Removal of outliers

Any observation over three times the median absolute deviations (MAD) away from the median is considered a measurement error and termed as an outlier. The outliers are replaced with the value generated by the piecewise cubic spline interpolation.

4.1.2. Removal of trend

The observations from the field typically have an upward or downward trend of the mean temperature. A first-order 'detrend model is used to remove the trend from the observation.

$$Y_{p,q} = O_{p,q} - T_{q,1} \times O_{p,q} \tag{8}$$

where the p is the number of nodes along depth, q is the number of nodes in time-series, $O_{p,q}$ is the matrix of the training data set and $T_{q,1}$ is the matrix of the de-trending parameters and $Y_{p,q}$ is the refined observations. When the calibrated solutions are used to make predictions, the trend values are required to be included. The estimated trend values using the parameters $T_{q,1}$ are added back using the relation $T_{q,1} \times O'_{p,q}$; where $O'_{p,q}$ is the predicted observation matrix.

4.2. Quantification of the error

The accuracy of the curve fittings are measured using the following error formulas:

4.2.1. Standard error of estimates (SSE)

The SSE (Eq. (9)) measured the mean deviation between the fitted value and measured value.

$$\mathrm{SEE} = \sqrt{\frac{\sum_{t=1}^{N}[o(t) - \hat{o}(t)]^2}{N-2}} \tag{9}$$

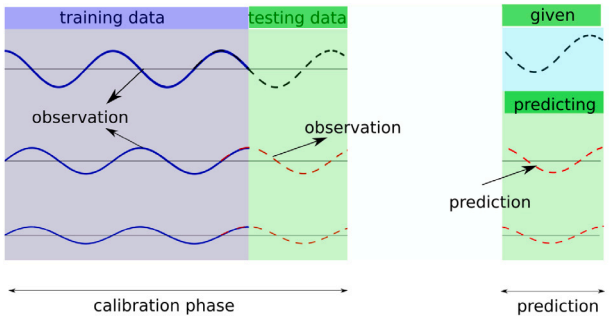

Fig. 9. 80% of the points in the time-series are used as training data (see Table 4 for details). The parameters are calibrated using the training data set. Then one observation at or near the surface is used to predict the temperatures within the soil in the testing data-set domain. Thus we obtain a predicted data set. The predicted data-set is compared with the testing data set to decide if the calibration is acceptable. If not, we re-calibrate.

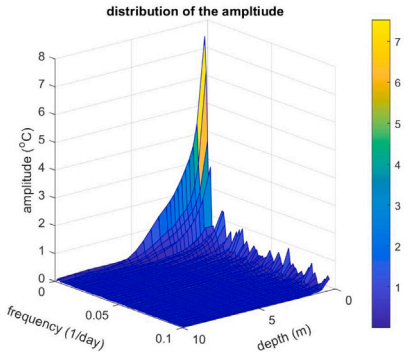

Fig. 10. The FFT analysis on the bh2 time series. The amplitude distributions over the frequencies and depth are shown. The highest amplitudes are found at the lower frequencies; also, the amplitudes reduce exponentially along with the depth. The phase of the Fourier components are randomly distributed and no relation between frequencies and depth can be found.

where, N is the number of the samples, $\hat{o}(t)$ is the observed N values, $o(t)$ is the value estimated by the model (either sine curve fitting or by Fourier analysis).

4.2.2. Coefficient of determination (R^2)

The value of R^2 indicates the part of the variance in the dependent variable, which we can estimate from the independent variables. However, the value of R^2 does not indicate whether appropriate regression was used.

$$\mathrm{R}^2 = 1 - \frac{\sum (o_i(t) - P_i(t))^2}{\sum (o_i(t) - \bar{o})^2} \tag{10}$$

where o_i is the ith observation, P is the prediction of the statistical model and $\bar{o}$ is the average of the observation.

4.2.3. Root Mean Square Error (RMSE)

Root-mean-square error (RMSE) measures the differences between the fitted curve/line values and the values observed. The following equation was used to calculate RMSE.

$$\mathrm{RMSE} = \sqrt{\frac{\sum_{n=1}^{T} \left(\hat{o}_t - o_t\right)^2}{N}} \tag{11}$$

5. Result and discussion

5.1. Preparation of training and testing data

The field observations mentioned in Table 3 are used to both calibrate and validate the solution. The observations are divided into two groups: training and testing data-sets, as shown in the Fig. 9 and detailed in Table 4. The purpose of the testing data-set is to compare the output after calibration. For this study, we used 80% of the time-length of the observations as training data-set and the remaining 20% for testing data-set. The maximum days of the testing data-set is 178 days for bh2, and the minimum is 80 days for bh6, which we believe is enough to compare and estimate the errors. We could even use a higher percentage of the data-set to train the model since our problem poses no probability of a common error in machine learning: over-training. The training data-sets are used to calibrate the parameters of the Eq. (5). Then only one observation at the topmost node for the time series is used to predict the temperatures at various depths, thus obtaining the predicted data-set. An error estimate is made comparing the observation in the testing data-set with the predicted data-set.

5.2. Calibration using training data-set

For every time series, there are 5 to 20 measurements at the nodes at different depths (detailed in Table 3). We retrieve the time series of the measurements at a 12-hour interval. Since the daily temperature variations cannot be captured when measured at 12-hour intervals, we convert the measurements to daily averages assuming that the average of the two 12-hour interval measurements represents the daily average temperature. The calibration starts with the Fast Fourier Transformation(FFT) analysis of the training data set. The output of FFT analysis on the bh2 time series is shown in Fig. 10 as an example. The amplitude distribution shows that peak amplitude (n = 1) are always at the lower frequencies. The amplitude reduces exponentially along with the depth. The smaller amplitudes are found at the higher frequencies representing the smaller daily variations of the temperature. A summary of the amplitude and frequency distributions for all the time series are shown in the Fig. 11. We notice that the peak frequencies of each series do not change along with the depth; it remains almost constant. However, the peak frequencies are not related to 365 days; rather, the time period ranges from 373 to 442 days. When a single sine-wave was fitted, the time period was always found to be 365 days. But when the time series is decomposed with FFT, the peak time periods are always found to be greater than 365 days. An amplitude and frequency distribution along the depth is drawn (Fig. 12). The related parameters are described in Tables 5 and 6. The amplitudes ($T_{a_n} : n = 1, 2, 3....$) decays exponentially over the depth. An exponential curve $a \cdot e^{-bz}$ with two parameters a and b fits the amplitudes distributions over the depth (see the distribution of the peak frequency in Fig. 12). The results for the top three peak amplitudes are summarised in Table 6. We notice that for n = 1, the highest peaks, the curve fittings have better R^2 values, however, not all the curve fitting has a high R^2 value, a value of 0.623 is also observed.

5.2.1. Phase-lags estimated from Cross Power Spectrum Density (CPSD) analysis

Cross Power Spectral Density (CPSD) was used to determine the true phase-lags between the signals at different depths. For a time series, CPSD between the top layer and that time series provides the cross power spectral density (CPSD) of the two signals, using *Welch's averaged, modified periodogram method* (Welch, 1967) of spectral estimation. The phase difference is estimated as multiples of the π, which is converted to days as the maximum phase lag 2π is equivalent to 365 days; shown in Fig. 13. As the analytical solution suggests, the phase lag increases over depth. A linear equation: $a + m \cdot z$ is fitted for each time series. The estimated values of the parameters are given in Table 6. The R^2 values suggest the relationship is well described by a linear equation.

Table 4
The observations are divided into two groups: training and testing. 80% of the data resides in the training data-set while the rest is put on the testing data-set.

Time series	Training data-set			Testing data-set		
	from	to	total days	from	to	total days
bh2	13-09–16	18-09–18	705	18-09–18	10-02–19	178
bh3	13-09–16	21-09–17	373	21-09–17	22-12–17	94
bh51	09-06–14	18-05–16	710	18-05–16	11-09–16	116
bh52	12-11–16	29-04–18	534	29-04–18	09-09–18	133
bh61	09-06–14	24-04–15	320	24-04–15	13-07–15	80

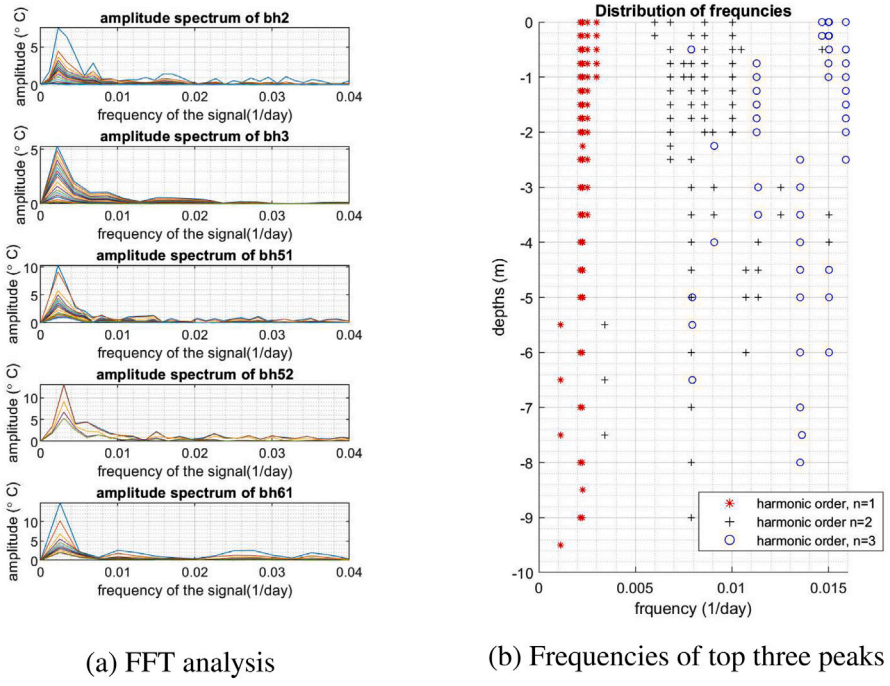

Fig. 11. (a) Fast Fourier Transformation (FFT) performed on time series reveals the low frequencies are the dominating signal. (b) Frequency distributions of the peak harmonic function (where n = 1 means the highest peak). The analysis shows the depth has no apparent effect on the frequencies. For the highest harmonic function, ranked n = 1, the frequencies are almost similar for all the time series till 5 m depth, after that some minor variations are noticeable. As for the next ranked frequencies, the range gets bigger. The spreading looks random for the n = 3.

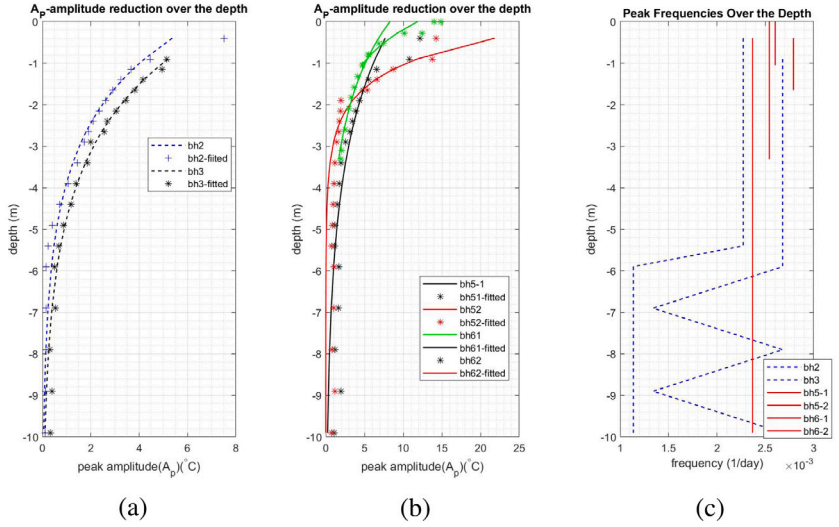

Fig. 12. The peak amplitude A_p for the n = 1, the peak frequency over the depth are depicted. The amplitude reduction is exponential; however, the frequency reduction is not observed till 5 m. The peak amplitudes at depth over 5 m are quite small (less than 1 °C).

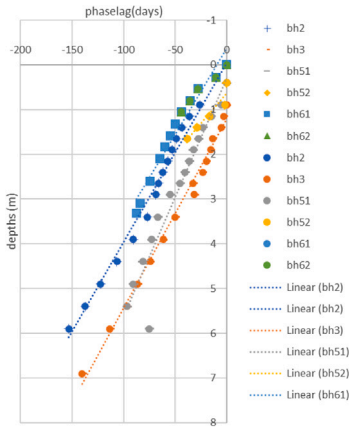

Fig. 13. The phase-lag over the depth shows a linear relation. The parameters of the curve fittings are mentioned in Table 6.

Table 5
An exponential curve ($a \cdot e^{-bz}$) is fitted to the amplitude distributions along the depth (where z is the depths). Only the top three harmonic functions are shown in the table.

Time series	Parameter	Rank of the peaks (n)		
		n = 1	n = 2	n = 3
bh2	a	6.514121	3.667414	1.746538
	b	0.79755	1.32577	1.46048
	R^2	0.990179	0.98182	0.994857
bh3	a	7.645913	1.381951	1.203991
	b	0.81458	0.623	0.91589
	R^2	0.992195	0.72056	0.581092
bh51	a	8.886689	3.962007	1.80939
	b	0.60695	0.91638	0.95682
	R^2	0.859604	0.679586	0.856837
bh52	a	27.27702	7.32094	1.574875
	b	1.64306	2.22973	0.1253
	R^2	0.877128	0.877806	0.95058
bh61	a	8.281672	1.419823	1.589165
	b	0.50868	0.74842	1.25615
	R^2	0.973705	0.942894	0.991782

Table 6
Phaselags of the signal determined by CPSD analysis, fitted to linear equation $a - mz$.

Time series	a	m	lags(days/m)	R^2
bh2	−0.0310	0.0399	25.0403	0.980723
bh3	1.2221	0.0420	23.7847	0.991341
bh51	0.3061	0.0530	18.8733	0.923127
bh52	0.1039	0.0447	22.3904	0.836632
bh61	−0.1459	0.0350	28.5465	0.959164

5.2.2. Discussion on the calibration of the parameters

The following observations are made:

- For a particular frequency, the amplitude decreases exponentially over the depth (see Figs. 10 and 12). The dominant amplitudes reside at the lower frequencies. For most cases, the first few peaks are significantly higher than the rest (see Fig. 11a). As expected, the longer the original signal, the stronger the peaks at the higher frequency (noticeable for bh5-1), indicating the model will be prone to errors if the higher frequencies are ignored.
- The frequency of the peak amplitude remains constant along the depths (see Fig. 11a). However, the peak frequencies are not the same for all boreholes. The observation suggests that the time period or seasonal variability has certain intervals and does not change within a short time.
- It is also observed that the highest amplitudes are found in the first peaks (see Fig. 11a). In other words, the peak with the highest time period also has the highest amplitude.

5.3. Validation of calibrated parameters and the solution using testing data-set

After calibrated using the training data sets, the parameters are used to predict the remaining 20% of the testing data set. In this section, we discuss the predictions and assess the errors. The Fourier components are determined from the training data set. The amplitude distributions are found from the Fourier components over the depth for each frequency. An exponential curve is fitted to relate the amplitude reduction over the depth for each frequency. Once the parameters are estimated, a prediction of the testing data set can be made. One example of the prediction is shown in Fig. 14. Along the x-axis, predicted temperatures and along the y-axis observed temperature are drawn. For a perfect prediction, the dots will be placed along the blue line which is drawn at a 45°. Any deviation from the line indicates an error in the estimation. Only the bh2 time series is shown in the Fig. 14. The rest of the time series can be found in Appendix E. The errors of the estimations are drawn along the depth in the sub-figures.

The following observations are made:

- The models has quite a high error at the top layers. The high RMSE errors indicate the predictions model breaks down at the organic active layer.
- When single sine-waves were fitted along with the time series, it was found that sine-wave deviates from the observations at the summer peak temperatures; the observations were lagged and smaller in amplitude. In contrast to the single sine-waves, when a combination of the harmonic wave functions is used, the errors are more prominent at the lower peaks. i.e. during winter. In other words, the summer temperatures are underestimated, whereas the winter temperatures are overestimated.

6. Conclusion

Soil temperature measurements are available at the Arctic coasts in the Kara Sea, Russia. The beach consists of continuous permafrost. The study area has two distinct zones, S#1 with low 5 m high cliffs and S#2 with 12–15 m high cliffs. Boreholes are constructed and thermal strings are placed inside them to measure the temperature until the depth of 9.9 m. The seasonal temperature variations are observed to be periodic. The time series of the temperature measurements are modelled with the boundary conditions as a combination of the harmonic waves. In this study, we calibrated the parameters of the solutions and validated the analytical solutions.

The salient outcome of the analysis can be summarised as follows:

- The seasonal variation of the temperature in the soil can be represented by the sine wave or combination of sine waves. The amplitude of such sine waves decreases exponentially. After 5 m of depth, the seasonal variations are small (less than one degree Celsius); we can neglect the variation.
- At the core of the pattern-seeking algorithm of the data-driven model is the analytical solution of the conduction–convection heat transfer equation. For the analysis, we calibrated the parameters only considering the depth-averaged values. But we notice that the errors created with such assumption are within the acceptable limit. The solution can be used to model a large area of the coast.
- The local variations of the solution's parameters are captured within one single parameter, RR in Eq. (6) for each frequency, i.e. for each observation at a certain location, the value of RR is different. The smaller frequencies capture the effect of the heat sink or sources, such as latent heat of phase changes.

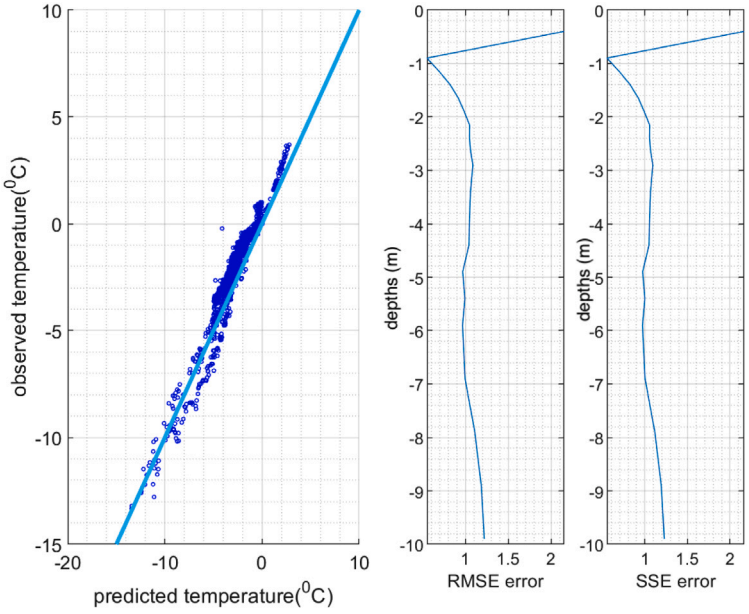

Fig. 14. Observed and predicted values are shown in the figures. A 45° line (thick blue) is drawn on the sub-figure to the left. The rest of the time series are shown in Appendix E. (For interpretation of the references to colour in this figure legend, the reader is referred to the web version of this article.)

- The phase-lag between the time series near the surface and the deeper part in the soil is considerable. The low thermal conductivity at the organic-active layer is one of the significant factors for the phenomenon. The summer high temperature of the soil at a depth of 5 m is almost 100 days behind that of surface temperature (see Fig. 13). The analytical model suggests the phase-lag should have a linear relation with depth. The observations from the field confirm the linear relation. The phase lag is estimated to be around 20 to 25 days per metre of depth.
- Zone S#2 has higher RR values and a lower water table, indicating very low to negligible heat transfer via convection. The error of the solutions is quite high in the shallow layers where surface run-off and precipitation during the summer is significant.
- The deviations from the observed values are most prominent at the positive temperatures, i.e. during summer. The solutions fail to capture the peak temperatures of the summer accurately.

The model did not consider the temperature profiles near the end of the cliffs, where the effect of the exposed bluff face on the temperature profile can be captured. Unlike the soil inside the cliffs, the crest and bluff-face are exposed to air on two planes. The temperature profiles will require corrections when the heat flows in two dimensions (2D). The precipitation and surface runoff from the flow of water of the thawing lakes were not considered. A separate model may be required to model the vegetation cover on the surfaces. The vegetation not only works as a blanket for the thermal energy transfer also works as cementing material against soil erosion.

Funding

This research was funded by the EU H2020-funded Nunataryuk project, where it is filed as part of deliverable 6.4.

CRediT authorship contribution statement

Mohammad Akhsanul Islam: Conceptualization, Methodology, Software, Formal analysis, Visualization, Writing:Original Draff, Writing - Review & Editing. **Raed Lubbad:** Conceptualization, Formal analysis, Investigation, Writing - Review & Editing, Supervision, Project administration, Funding acquisition. **Seyed Ali Ghoreishian Amiri:** Formal analysis, Investigation, Software. **Vladislav Isaev:** Data curation, Investigation, Resources, Validation, Writing - Review & Editing, Supervision, Project administration. **Yaroslav Shevchuk:** Data curation, Investigation. **Alexandra Vladimirovna Uvarova:** Data curation, Investigation. **Mohammad Saud Afzal:** Validation, Writing - Review & Editing, Supervision, Funding acquisition. **Avinash Kumar:** Validation, Writing - Review & Editing, Supervision, Funding acquisition.

Acknowledgements

The report is written as part of the EU H2020-funded Nunataryuk project, where it is filed as part of deliverable 6.4, and by the NC-POR//PACER Outreach Programme (POP) Initiative on “Predictive Tools for Arctic Coastal Hydrodynamics and Sediment Transport”. This research is also supported by Sustainable Arctic Marine and Coastal Technology (SAMCoT), Norway, Norwegian University of Science and Technology (NTNU), Lomonosov Moscow State University (MSU), Russia and Sponsored Research and Industrial Consultancy (SRIC), Indian Institute of Technology Kharagpur.

Appendix A. Supplementary data

Supplementary material related to this article can be found online at https://doi.org/10.1016/j.polar.2021.100732.

References

Andersland, O.B., Ladanyi, B., et al., 2003. Frozen Ground Engineering. John Wiley & Sons.

Are, F., 1988. Thermal abrasion of sea coasts (part i). Taylor & Francis.

Barnhart, K.R., Anderson, R.S., Overeem, I., Wobus, C., Clow, G.D., Urban, F.E., 2014. Modeling erosion of ice-rich permafrost bluffs along the alaskan beaufort sea coast. J. Geophys. Res. Earth Surf. 119 (5), 1155–1179.

Bernstein, L., Bosch, P., Canziani, O., Chen, Z., Christ, R., Riahi, K., 2008. IPCC, 2007: climate change 2007: synthesis report. IPCC.

Gao, Z., Fan, X., Bian, L., 2003. An analytical solution to one-dimensional thermal conduction-convection in soil. Soil Sci. 168 (2), 99–107.

Gao, Z., Lenschow, D.H., Horton, R., Zhou, M., Wang, L., Wen, J., 2008. Comparison of two soil temperature algorithms for a bare ground site on the loess plateau in China. J. Geophys. Res.: Atmos. 113 (D18).

Guégan, E., 2015. Erosion of permafrost affected coasts: rates, mechanisms and modelling. NTNU.

Holmes, T., Owe, M., De Jeu, R., Kooi, H., 2008. Estimating the soil temperature profile from a single depth observation: A simple empirical heatflow solution. Water Resour. Res. 44 (2).

Hoque, M.A., Pollard, W.H., 2009. Arctic coastal retreat through block failure. Can. Geotech. J. 46 (10), 1103–1115.

Hu, G., Zhao, L., Wu, X., Li, R., Wu, T., Xie, C., Qiao, Y., Shi, J., Li, W., Cheng, G., 2016. New fourier-series-based analytical solution to the conduction–convection equation to calculate soil temperature, determine soil thermal properties, or estimate water flux. Int. J. Heat Mass Transfer 95, 815–823.

Isaev, V., Kioka, A., Koshurnikov, A., pogorelov, a., Amangurov, R., podchasov, o., Sergeev, D., 2016. Field investigation and laboratory analyses; baydaratskaya bay 2016. http://dx.doi.org/10.13140/RG.2.2.13836.00645.

Isaev, V., Koshurnikov, A., Pogorelov, A., Amangurov, R., Podchasov, O., Sergeev, D., Buldovich, S., Aleksyutina, D., Grishakina, E., Kioka, A., 2019. Cliff retreat of permafrost coast in south-west baydaratskaya bay, kara sea, during 2005–2016. Permafr. and Periglac. Process. 30 (1), 35–47.

Kobayashi, N., Vidrine, J., Nairn, R., Soloman, S., 1999. Erosion of frozen cliffs due to storm surge on beaufort Sea Coast. J. Coast. Res. 332–344.

Lantuit, H., Pollard, W., 2008. Fifty years of coastal erosion and retrogressive thaw slump activity on herschel island, southern beaufort sea, yukon territory, Canada. Geomorphology 95 (1–2), 84–102.

Leont'yev, I., 2003. Modeling erosion of sedimentary coasts in the western Russian arctic. Coast. Eng. 47 (4), 413–429.

Leont'yev, I., 2004. Coastal profile modeling along the Russian arctic coast. Coast. Eng. 51 (8–9), 779–794.

Lewkowicz, A., 1991. Climatic change and the permafrost landscape, In: Arctic Environment: Past, Present and Future, In: Woo, MK and Gregor, DJ(Ed.), Proceedings of a Symposium, pp. 14–15.

Nairn, R., Solomon, S., Kobayashi, N., Virdrine, J., 1998. Development and testing of a thermal-mechanical numerical model for predicting arctic shore erosion processes. In: Permafrost: Proceedings of the Seventh International Conference, Yellowknife, NWT, June 23-27. Centre d'études nordiques, Université Laval, Québec, Canada, pp. 789–795.

Ogorodov, S., Aleksyutina, D., Baranskaya, A., Shabanova, N., Shilova, O., 2020. Coastal erosion of the Russian arctic: An overview. J. Coast. Res. 95 (sp1), 599–604.

Plaxis, 2021. Manuals:plaxis. https://communities.bentley.com/cfs-file/_key/communityserver-wikis-components-files/00-00-00-05-58/PLAXIS2DCE_2D00_V21.00_2D00_04_2D00_Scientific.pdf. (Accessed 25 July 2021).

Ravens, T.M., Jones, B.M., Zhang, J., Arp, C.D., Schmutz, J.A., 2012. Process-based coastal erosion modeling for drew point, north slope, alaska. J. Waterw. Port Coast. Ocean Eng. 138 (2), 122–130.

Romanovsky, V., Osterkamp, T., 1997. Thawing of the active layer on the coastal plain of the alaskan arctic. Permafr. Periglac. Process 8 (1), 1–22.

Stallman, R., 1965. Steady one-dimensional fluid flow in a semi-infinite porous medium with sinusoidal surface temperature. J. Geophys. Res. 70 (12), 2821–2827.

Van Wijk, W.R., De Vries, D., 1963. Periodic temperature variations in a homogeneous soil. Phys. Plant Environ. 1, 103–143.

Verhoef, A., van den Hurk, B.J., Jacobs, A.F., Heusinkveld, B.G., 1996. Thermal soil properties for vineyard (EFEDA-i) and savanna (HAPEX-sahel) sites. Agricult. Forest Meteorol. 78 (1–2), 1–18.

Vijay, P., et al., 2018. Advances in Coastal Hydraulics. World Scientific.

Welch, P., 1967. The use of fast fourier transform for the estimation of power spectra: a method based on time averaging over short, modified periodograms. IEEE Trans. Audio Electroacoust. 15 (2), 70–73.